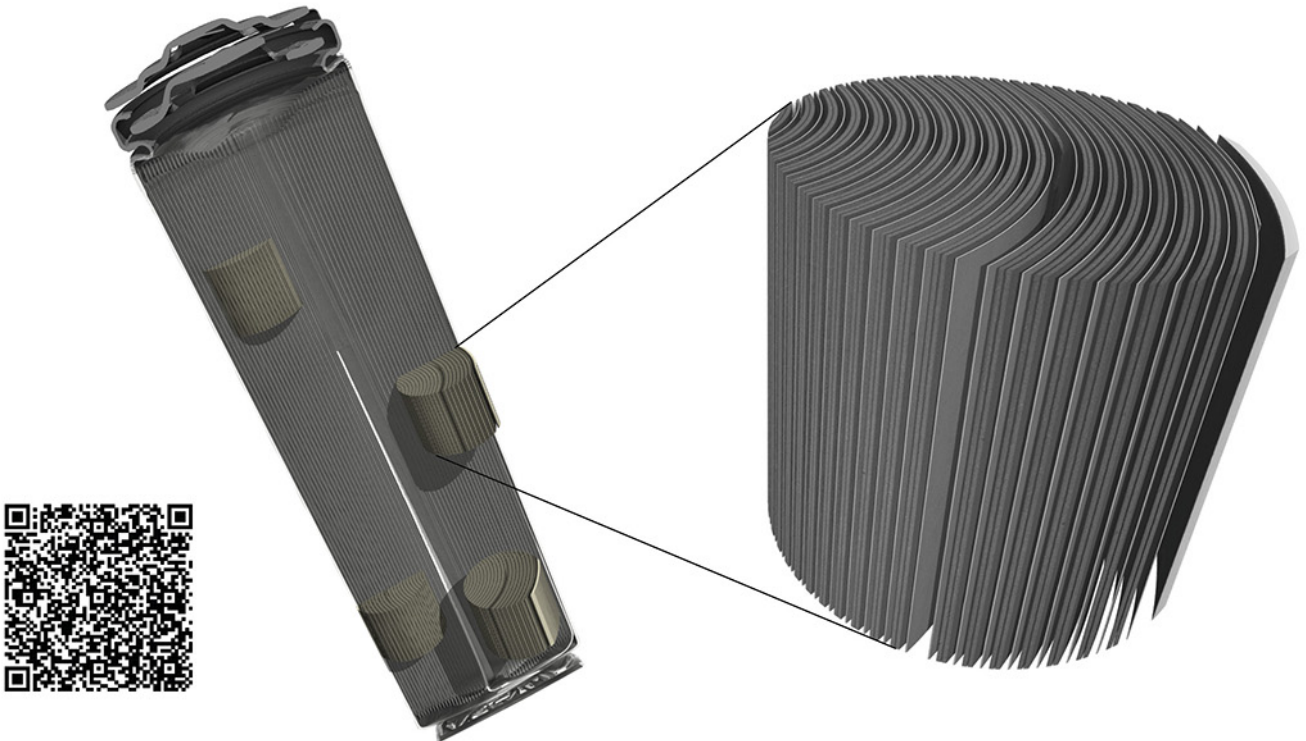# TESCAN micro-CT solutions for energy storage materials research

TESCAN UniTOM XL

- ✓ Multi-scale non-destructive 3D imaging optimized to maximize throughput and contrast
- ✓ Fast scanning and high sample throughput with temporal resolutions below 10 seconds
- ✓ Wide array of samples types
- ✓ Enables dynamic tomography and *in-situ* experiments
- ✓ Dynamic screening for synchrotron beamtime
- ✓ Modular and open system with unmatched flexibility for research

Click and find out more

Direct Observation of Reductive Coupling Mechanism between Oxygen and Iron/Nickel in Cobalt-Free Li-Rich Cathode Material: An in Operando X-Ray Absorption Spectroscopy Study

Ditty Dixon,* Stefan Mangold, Michael Knapp, Helmut Ehrenberg,* and Aiswarya Bhaskar*

Li-rich cathodes possess high capacity and are promising candidates in next-generation high-energy density Li-ion batteries. This high capacity is partly attributed to its poorly understood oxygen-redox activity. The present Li-rich cathodes contain expensive and environmentally-incompatible cobalt as a main transition metal. In this work, cobalt-free, iron-containing Li-rich cathode material (nominal composition $Li_{1.2}Mn_{0.56}Ni_{0.16}Fe_{0.08}O_2$) is synthesized, which exhibits excellent discharge capacity ($\approx$250 mAh g^{-1}) and cycling stability. In operando, X-ray absorption spectroscopy at Mn, Fe, and Ni K edges reveals its electrochemical mechanism. X-ray absorption near edge structure (XANES) features of Fe and Ni K edges show unusual behavior: when an electrode is charged to 4.5 V, Fe and Ni K edges' XANES features shift to higher energies, evidence for $Fe^{3+}\rightarrow Fe^{4+}$ and $Ni^{2+}\rightarrow Ni^{4+}$ oxidation. However, when charged above 4.5 V, XANES features of Fe and Ni K edges shift back to lower energies, indicating $Fe^{4+}\rightarrow Fe^{3+}$ and $Ni^{4+}\rightarrow Ni^{3+}$ reduction. This behavior can be linked to a reductive coupling mechanism between oxygen and Fe/Ni. Though this mechanism is observed in Fe-containing Li-rich materials, the only electrochemically active metal in such cases is Fe. $Li_{1.2}Mn_{0.56}Ni_{0.16}Fe_{0.08}O_2$ has multiple electrochemically active metal ions; Fe and Ni, which are investigated simultaneously and the obtained results will assist tailoring of cost-effective Li-rich materials.

Dr. D. Dixon,[+] Dr. M. Knapp, Prof. H. Ehrenberg, Dr. A. Bhaskar[+]
Karlsruhe Institute of Technology (KIT)
Institute for Applied Materials (IAM)
Hermann-von-Helmholtz-Platz 1, D-76344 Eggenstein-Leopoldshafen, Germany
E-mail: ditty@cecri.res.in; helmut.ehrenberg@kit.edu; aiswarya@cecri.res.in
Dr. S. Mangold
Institute for Photon Science and Synchrotron Radiation (IPS)
Karlsruhe Institute of Technology (KIT)
Hermann-von-Helmholtz-Platz 1, D-76344 Eggenstein-Leopoldshafen, Germany
Prof. H. Ehrenberg, Dr. A. Bhaskar
Helmholtz Institute Ulm for electrochemical energy storage (HIU)
Helmholtzstrasse 11, D-89081 Ulm, Germany

The ORCID identification number(s) for the author(s) of this article can be found under https://doi.org/10.1002/aenm.202100479.

[+]Present Address: Electrochemical Power Sources Division, CSIR-CECRI, Karaikudi, Tamil Nadu, India, 630003

1. Introduction

Development of positive electrode (cathode) materials for Li-ion batteries, possessing high capacity is necessary to meet current energy requirements and hence to facilitate their commercial applications. The layered Li-rich materials with a general composition $xLi_2MnO_3 \cdot (1-x)$ $LiMO_2$ (M = Mn, Co, Ni, Fe) are attractive candidates as high-capacity cathode materials as they can deliver long term reversible capacities close to 200 mAh g^{-1} when cycled within the voltage range 2.0–4.8 V.[1–6] In the Li-rich layered materials, mixed transition metal/Li layers exist unlike in pure layered materials like $LiCoO_2$. The former layer will be separated from Li-only layers by oxygen layers. Due to the presence of Li on the transition metal layer, a superlattice ordering of the transition metal and lithium takes place, which lowers the symmetry of the Li-rich material to monoclinic $C2/m$ from $R\overline{3}m$.[3] It was first demonstrated in 1999 by Kalyani et al., that Li_2MnO_3 could be activated electrochemically in a Li-half cell by increasing the upper cut off voltage to 4.5 V.[7] When the initial research works were focused on purely manganese-containing layered Li-rich chemistries, later works mainly focused on Co and Ni-substituted layered Li-rich materials.[4,8–13] Additionally, Fe-substituted layered materials also received considerable attention from the '90s onwards, due to the low cost and wide abundance of Fe compared to Co and Ni.[6,14,–20] In 1993, Reimers et al., reported a work on a Fe and Ni containing layered material, $LiFe_yNi_{1-y}O_2$, which was found isostructural with $LiNiO_2$ in a selected composition range of $0 \leq y \leq 0.23$.[21] In another composition range of $0.23 \leq y \leq 0.48$, a coexistence of hexagonal ($LiFe_{0.23}Ni_{0.77}O_2$, with a cation mixing between lithium layers and transition metal, particularly Fe) and cubic phases ($LiFe_{0.48}Ni_{0.58}O_2$) were observed. The electrochemical cycling conducted between voltage range of 2.0–4.2 V reveals a decrease in the reversible capacity with increase in the iron content "y".[21] Fe-substituted Li_2MnO_3 was investigated as a 4 V cathode in lithium-ion cells in 2002, by Tabuchi et al.[22] The capacity delivered by the material was found to be influenced by the synthesis method, annealing temperature and voltage range applied. In situ Moessbauer spectroscopy investigations reveal the oxidation of Fe^{3+}

ADVANCED
SCIENCE NEWS

www.advancedsciencenews.com

ADVANCED
ENERGY
MATERIALS

www.advenergymat.de

to Fe^{4+} at approximately around ≈4 V during charging and vice versa on discharging.[22] In a later work published in 2005 by the same research group, the electrochemical performance of Fe-doped Li_2MnO_3 was improved by controlling the synthesis temperatures as well as by introducing various dopants like Al, Ni, and Co.[23] Fe- and Ni-substituted Li_2MnO_3 was investigated as a 3.5 V class cathode by Tabuchi et al., in 2011 in a full cell versus mesocarbon microbeads as negative electrodes (anodes). Various compositions were studied, where the stoichiometry amount of Fe and Ni are varied and they have concluded that careful optimization, which ends up in retaining a single phase monoclinic structure with maximized surface area is necessary to obtain the electrochemical performance for these materials at par with the existing cathode materials.[16] Several compositions for Fe- and Ni-substituted Li_2MnO_3 were reported such as $Li_{1.2}Mn_{0.32}Ni_{0.32}Fe_{0.16}O_2$,[24] $0.5Li_2MnO_3 \cdot 0.5LiMn_xNi_yFe_{(1-x-y)}O_2$, $(0.3 \leq x \leq 0.5, 0.4 \leq y \leq 0.5)$,[25] $Li_{1.2}Mn_{0.53}Ni_{0.13}Fe_{0.13}O_2$,[19] $Li_{1.20}Mn_{0.54}Ni_{0.13}Fe_{0.13}O_2$,[26] $Li_{1.2}Mn_{0.54}Ni_{0.087}Fe_{0.173}O_2$,[26] $Li_{1.2}Mn_{0.54}Ni_{0.173}Fe_{0.087}O_2$,[26] $Li(Li_{0.23}Mn_{0.47}Fe_{0.2}Ni_{0.1})O_2$,[27] $Li_{1.2}Mn_{0.56}Ni_{0.16}Fe_{0.08}O_2$,[28] $0.6Li_2MnO_3 \cdot 0.4Mn_{1/3}Ni_{1/3}Fe_{1/3}O_2$,[29] $Li_{1.2}Mn_{0.54}Ni_{0.22}Fe_{0.04}O_2$,[30] $Li_{1.26}Fe_{0.22}Mn_{0.52}O_2$,[20] $Li_{1.2}Mn_{0.6-0.5x}Ni_{0.2-0.5x}Fe_xO_2$ $(x = 0.06, 0.13, 0.2)$.[31] It was observed that increasing the concentration of Fe in Ni-doped Li_2MnO_3, results in increase in the onset potential of the irreversible peak appearing in cyclic voltammetry during charging.[25] Moreover, Fe-doping in small amount was observed to broaden the interslab distance in the layered structure, which further enhances Li^+ transport kinetics, thereby resulting in high reversible capacity and stable cycling.[25]

There were intense investigations conducted on the electrochemical mechanism of layered Li-rich cathode materials, particularly of those containing Co. In literature, different results and speculations exist regarding the first charge mechanism in these Li-rich layered materials. According to some of the literature reports, the Li_2MnO_3 component of this material loses Li^+ and a corresponding amount of oxygen, in the first charge at ≈4.5 V, resulting in a net loss of "Li_2O", and forms electrochemically active layered MnO_2-like species.[4,9,32,33] The newly formed MnO_2 species is able to intercalate Li^+ in the subsequent cycles. In addition, in situ X-ray absorption spectroscopy (XAS) investigations reported by Rana et al. reveals conversion of the MnO_2-type structure to a Li_2MnO_3-type structure when Li^+ ions are inserted during discharge.[34,35] Tran et al., observed that during the oxygen and Li losses in a material with composition $Li_{1.12}(Ni_{0.425}Mn_{0.425}Co_{0.15})_{0.88}O_2$, the transition metal ordering in the slabs will be lost and results in cation redistribution.[36] They attribute this rearrangement to a migration of transition metal ions from the transition metal sites to the vacancies formed by Li deintercalation. Charge compensation mechanism of cobalt-free Li-rich cathode material $Li_{1.2}Ni_{0.2}Mn_{0.6}O_2$ was investigated by Shimoda et al., in 2020 using synchrotron diffraction, XAS, and nuclear magnetic resonance spectroscopy techniques.[37] During charging, the a-axis was found to contract and the c-axis was found to elongate as a result of Ni oxidation during the slope region of the voltage profile. However, in the plateau region, lattice parameter variation was found to be negligible, suggesting charge compensation by oxygen anions by formation of ligand holes, peroxide-like moieties or O_2 release. Further, a partial reduction of Ni

was also observed during charging, at higher voltage, indicating the redox coupling of Ni and O. At the end of discharge, Ni^{2+} was observed predominantly in the material. No such redox coupling was observed for Mn in the material due to the preferential hybridization of Ni over Mn with activated oxygen species formed at high potentials, because of the increased electronegativity of Ni ion. The reversibility of this oxygen redox was found to be dependent on the Li-richness and the transition metal ion present.[38] Ni stabilizes reversible oxygen redox by suppressing oxygen loss from the structure in comparison with Co. Coexistence of Ni and Co in Li-rich materials was revealed to suppress the oxygen loss more efficiently than that contain Co but not Ni. The mechanisms of oxygen loss suppression were proposed as; core shell structure formation, and solid-solution formation. Compositional tuning, particularly by increasing Ni content was found to control oxygen redox as reported very recently by Yin et al.[39] Introduction of a stepwise precycling treatment was found to suppress the oxygen release during activation in a $Li_{1.26}Mn_{0.52}Fe_{0.22}O_2$ cell with graphite as counter electrode. With the aid of ex situ XAS and X-ray photoelectron spectroscopy (XPS), the main charge compensation mechanism was revealed to be a redox reaction of O^{2-} to form O_2^{2-}, in addition to the expected transition metal redox reaction.[40]

In the initial ex situ XAS investigations conducted on $LiFeO_2$-Li_2MnO_3 solid solution at the Mn K edge, a difference in the line shapes was observed for the pristine and charged samples.[22] However, the energy positions of the peak maxima and threshold were similar for both samples, revealing that the oxidation of Mn^{4+} to higher oxidation states would not have taken place. The origin of this line shape change was unclear then. Nevertheless, at the end of the discharge process (at ≈2.5 V), a peak shift close to $LiMnO_2$ threshold was observed, indicating reduction of Mn^{4+} to Mn^{3+}.[22] An ex situ XAS analysis conducted on $(Li_{1+x}[(Fe_{1/2}Ni_{1/2})_yMn_{1-y}]_{1-x}O_2, 0 < x < 1/3, 0.2 \leq y \leq 0.8)$ samples revealed a dependence of the Ni oxidation state on the material composition.[15] Meanwhile, Mn K edge XANES spectra displayed the character of Li_2MnO_3, irrespective of the material composition.[15] Fe^{57} Moessbauer spectra obtained for the samples reveal the presence of the Fe component mainly in its high-spin trivalent state. Small amounts of tetravalent Fe were also visible in some of the pristine compositions, which were found to be dependent on the calcination temperatures and atmosphere. In 2008, Kikkawa et al., investigated the Li^+ extraction and insertion behavior in Li_2MnO_3-$LiFeO_2$, otherwise represented as $Li_{1.2}Mn_{0.4}Fe_{0.4}O_2$, in real space using a spectrum-imaging scheme based on scanning transmission electron microscopy-electron energy-loss spectroscopy.[41] For this, four samples; one before charging, one partially charged, one completely charged, and one after discharge were prepared ex situ. Mn- and Fe-rich regions were found to coexist, indicating the presence of Li_2MnO_3-like and α-$LiFeO_2$-like regions within a common oxygen sublattice. Further, it was observed that, during the initial charging, Li extraction occurs from the α-$LiFeO_2$-like regions, followed by the oxidation of the trivalent transition metal ions. The extra charge capacity observed during the first charge was attributed to the oxidation of oxygen ions in Li_2MnO_3-like regions.[41] Ex situ XPS and XAS investigations revealed the redox reaction of oxygen (O_2 to O_2^{2-} conversion) as the major charge compensation mechanism during the

precycling and not the redox reaction of transition metals. Mn was found to remain in its tetravalent form during charging, irrespective of the electrochemical treatment, indicating the inactivity of Mn ions in Fe-containing Li-rich compounds.[40] An ex situ X-ray diffraction analysis proposes a first charge mechanism involving oxygen loss at the surface and reversible oxygen oxidation in the bulk of the Li-rich material.[42] Gent et al. have proposed that it is possible to tune the voltage of anion redox and the stability of the Li-rich material by controlling the transition metal migration pathways.[43] Ex situ XAS and soft XAS investigations conducted on $0.7Li_2MnO_3$-$0.3LiFeO_2$ revealed a change in the valence states of Mn ions from tetravalent to tri/divalent state near the surface, followed by the removal of oxygen and lithium. Hence, the main charge compensation mechanism was found to be redox reaction of Mn and oxygen ions, in addition to the Fe^{4+}/Fe^{3+} redox reaction.[44] In the Li-rich layered materials with nominal composition Li_2MnO_3-$LiMO_2$, the coexistence of cation elements M other than Mn such as Ni, Co, etc., are found to have a significant role in sustaining an effective coordination structure facilitating the oxygen-anion redox reactions.[45] Participation of Fe^{4+}/Fe^{3+} redox couple was observed in $Li_{1.2}Ni_{0.13}Fe_{0.13}Mn_{0.54}O_2$ using XPS which is further supported by first principle calculation.[2] In operando XAS investigations conducted on $Li_2Ru_{0.75}Fe_{0.25}O_3$ reveal the existence of Ru in +4 and Fe in +3 oxidation states, respectively in the pristine sample.[46] Ru^{4+} was found to undergo oxidation during charge until ≈3.75 V. The process was found to be reversible during cell discharge. The change in the pre-edge feature of the Fe K edge during charge was attributed to strong changes in Fe coordination environment. The pre-edge feature did not return back to its original value during discharging, indicating a permanent distortion of the Fe-octahedra. The possible explanation for this distortion was given as oxidation of Fe^{3+} to Fe^{4+} during the removal of the second Li^+ from the host structure around 4 V, resulting in the reorganization of the oxygen network, forming $2O^{1-}$ species, further leading to an oxygen network reorganization.[46] The oxygen redox activity is found to be directly influenced by the type of transition metal present in the Li-rich oxide.[47] For example, $Li_{1.2}Ni_{0.2}Mn_{0.6}O_2$ containing the 3d transition metal Ni was found to exhibit oxygen redox activity at higher voltages, which was found to be absent in its Ru (4d transition metal) analog, $Li_{1.2}Ni_{0.2}Ru_{0.6}O_2$. In $Li_{1.2}Ni_{0.2}Ru_{0.6}O_2$, both Ni and Ru undergo oxidation during charging, while in $Li_{1.2}Ni_{0.2}Mn_{0.6}O_2$, only Ni undergoes oxidation and Mn remains in +4 oxidation state. The extra capacity observed for this material is resulting from the oxygen redox activity. However, there is still a lack of information regarding the electrochemical mechanism in Li-rich materials containing Mn, Fe, and Ni, where both Ni and Fe are supposed to be electrochemically active especially when the coexistence of Ni and Fe are found to be beneficial for the electrochemical performance.

Herein, an Mn-based Li-rich layered material containing electrochemically active Ni and Fe, $Li_{1.2}Mn_{0.56}Ni_{0.16}Fe_{0.08}O_2$, is synthesized via a sol-gel process and the electrochemical mechanism was elucidated using multiple edge (Ni, Fe, and Mn) in operando XAS investigations in real-time for the same cell. By doing so, the loss of information arising from preparing ex situ samples as well as using different cells for different edges can be avoided. This will further increase the reliability of

the electrochemical mechanism elucidated. The details will be discussed in the latter text.

2. Results and Discussion

2.1. Structural Characterization Using Synchrotron Diffraction

The Rietveld refinement results based on the obtained synchrotron diffraction patterns for the Fe-LIR sample are displayed in **Figure 1**a. The 2θ region where the superlattice reflections appear was not considered in the Rietveld refinement analysis since the Fullprof program is unable to completely model the nanocomposite structure of the Li-rich layered structures and is zoomed in as shown in the inset of Figure 1a.[48] These superstructure reflections are indicative of presence of Li on the transition metal layers of the Li-rich material.[48] The diffraction pattern of Fe-LIR material displayed mainly two sets of
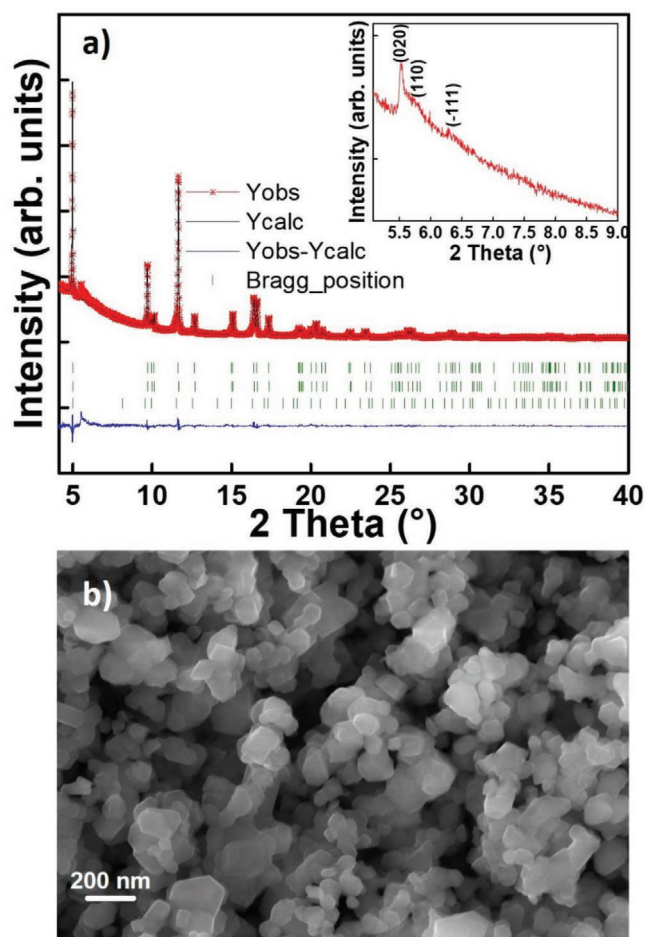

Figure 1. a) Rietveld refinement results based on the observed synchrotron diffraction patterns (wavelength $\lambda = 0.413486$ Å), of as prepared Fe-LIR. Note that the top two lines of reflection marks refers to the $R\bar{3}m$ space group (layered) and the last line of marks to the contribution from spinel-like impurity ($Fd\bar{3}m$ space group). The superlattice reflections arising from the layered Li-rich component, corresponding to the space group $C2/m$ are given in the inset. b) SEM image of as-prepared Fe-LIR sample.

**ADVANCED
SCIENCE NEWS**

www.advancedsciencenews.com

**ADVANCED
ENERGY
MATERIALS**

www.advenergymat.de

reflections belonging to the Li-rich layered phase, which could be indexed to $R\bar{3}m$ space group with slightly different unit cell parameters. The phase fractions of the two observed phases with $R\bar{3}m$ space group were 56(2)% and 33(1)%, respectively. In addition, an impurity phase was observed with a phase fraction of ≈10.1(4)%. This impurity phase could be assigned to a cubic spinel structure ($Fd\bar{3}m$ space group), where the 16c sites are also occupied. The percentage occupancy of the 16c site was obtained as 35%, after Rietveld refinement using the above-mentioned spinel structural model, keeping the occupancy of 16d sites fixed to 100%. The unit cell parameters obtained from Rietveld refinement are $a = b = 2.8660(2)$ and $c = 14.291(2)$ for the first phase and $a = b = 2.8590(2)$ and $c = 14.54(2)$ for the second phase, respectively. The structural parameters are summarized in Table S1, Supporting Information.

2.2. Morphology Analysis

A scanning electron microscopy (SEM) image of Fe-LIR is displayed in Figure 1b. The primary particles of Fe-LIR are agglomerated to form secondary particles as revealed from the image. Intergrown particles with a primary particle size distribution in the range of 50–150 nm were observed, with a mixture of hexagonal or close to sphere shape typical for Li-rich materials.[1]

2.3. Electrochemical Characterization

The cyclic voltammogram obtained for the Fe-LIR sample is displayed in **Figure 2**. A potential range 2.0–5.1 V versus Li⁺/Li was used for conducting the measurement with a scan rate of 0.1 mV s⁻¹. A peak is observed at ≈4.1 V in the first charge with a shoulder around 3.8 V, which could be attributed to $Fe^{3+}\rightarrow Fe^{4+}$ and $Ni^{2+}\rightarrow Ni^{4+}$ electrochemical reactions, respectively.[2,30] A second peak with higher intensity is observed at ≈4.6 V in the first charge which could be assigned to the

irreversible removal of oxygen and corresponding amounts of Li from the crystal lattice ("Li₂O" removal) of Li_2MnO_3 to form MnO_2-like structures.[49] This phase is reported as a Li-poor cubic spinel (λ-MnO_2) by Shimoda et al., using synchrotron diffraction investigation. In addition, another peak is observed at ≈5.0 V which cannot be well resolved from the ≈4.6 V peak. The exact origin of this peak is unknown but could be due to the electrolyte decomposition.

In the following discharge, no corresponding reduction peak was observed at ≈4.6 V which shows a completion of the activation of Li_2MnO_3 component. In addition, a broad peak is observed in the potential range of 3.8–4.4 V in the discharge, which could be attributed to the Li⁺ re-intercalation into the $LiFe_{0.2}Ni_{0.4}Mn_{0.4}O_2$ component of the Fe-LIR material, resulting in $Fe^{4+}\rightarrow Fe^{3+}$ and $Ni^{4+}\rightarrow Ni^{2+}$ electrochemical reactions.[2] Similar behavior was already reported in the case of Co-containing Li-rich positive electrode materials.[1,2] A new peak appears in the first discharge at ≈3.2 V which could be assigned to $Mn^{4+}\rightarrow Mn^{3+}$ electrochemical reactions from the MnO_2-like component.[2] Corresponding oxidation peaks were observed in the subsequent charge for both the aforementioned reactions which confirm their reversibility. Moreover, the electrochemical activity around ≈4.6 V was absent, further confirming the completion of the "Li₂O removal" in the first charge. The electrochemical activity corresponding to $Mn^{4+}\rightarrow Mn^{3+}$ reaction was shifted to lower potentials (close to ≈3.0 V) in the 24th cycle of Fe-LIR which may be attributed to any cation rearrangement occurring during cycling.[2]

The results from the galvanostatic cycling conducted in a potential range 2.00–4.95 V for the Fe-LIR material are displayed in **Figure 3**a and the corresponding voltage profiles for the first, second and 40th cycle are displayed in Figure 3b. The first three cycles were conducted at a charge-discharge rate of C/10 to get the complete activation of the Li_2MnO_3 component. A rate of C/5 was applied for the subsequent cycles. Note that the discharge capacity value of the first cycle performed with the charge–discharge rate C/5 (actual 4th cycle) is taken into account for the calculation of the capacity retention. An apparent high first charge capacity of ≈315 mAh g⁻¹ (at C/10) could be calculated for the Fe-LIR sample, from the number of electrons flown as derived from the integrated current, but the subsequent discharge capacity of 243 mAh g⁻¹ indicates that about 23% of these electrons take part in side reactions rather than reversible redox reactions. Hence, a coulombic efficiency of ≈77% could be calculated for the first cycle which is close to the values reported in literature for the Co containing Li-rich materials and is higher than those reported for the Fe containing Li-rich materials in some of the reports.[2,19] The discharge capacity was observed to be ≈206 mAh g⁻¹ for the Fe-LIR when the material was cycled at a rate of C/5 in the 4th cycle. A capacity retention of ≈94% was obtained in the 40th cycle. From the displayed voltage profiles it is observed that a major amount of the first charge capacity of the Fe-LIR material is delivered by the activation of the Li_2MnO_3 component, as revealed by the plateau at >4.5 V. After the first charge, increased slopes appear in the voltage profiles and the steady plateau disappears, indicating the complete transformation of the Li_2MnO_3 component in the first charge itself. A C/5 rate was applied from cycle 4. A comparison of the 4th and 40th cycle profiles reveals a shift in
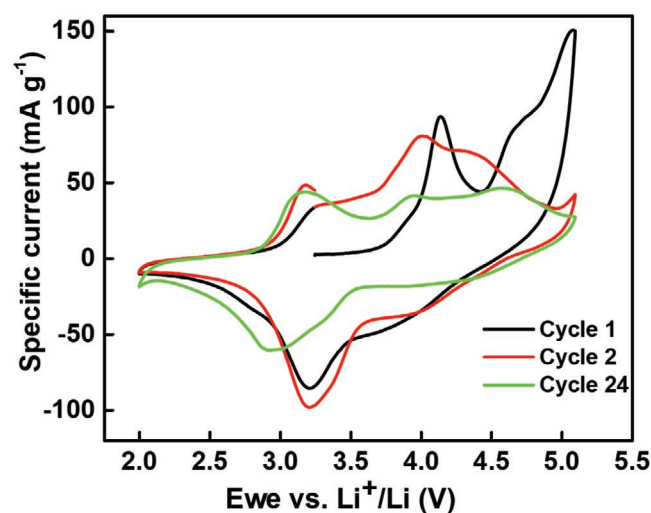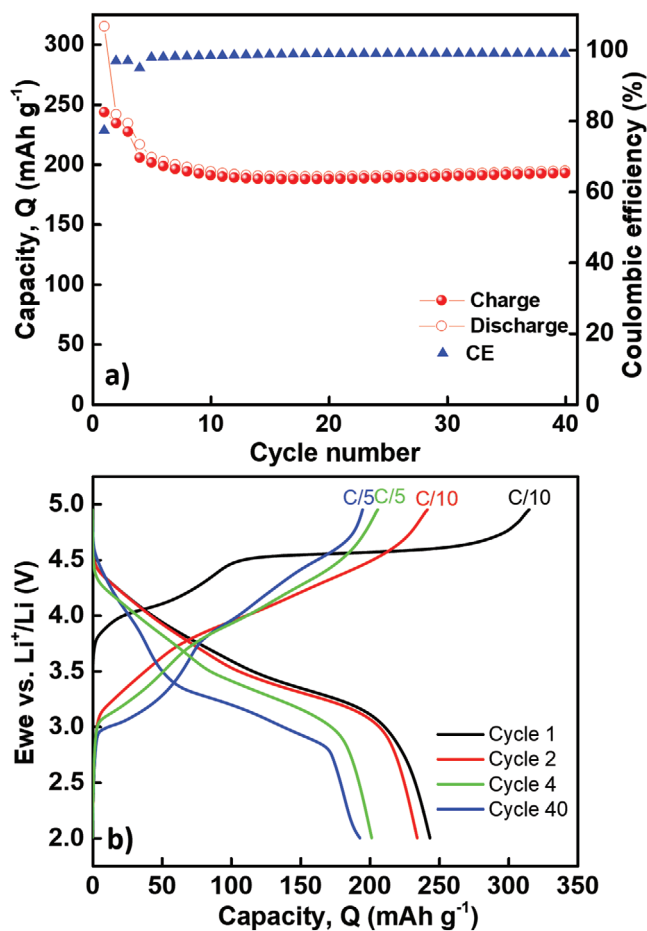

Figure 2. Cyclic voltammograms of the Fe-LIR sample, done with a scan rate of 0.1 mV s⁻¹, showing first, second and 24th cycles (potential range 2.0–5.1 V versus Li⁺/Li).

**ADVANCED
SCIENCE NEWS**

www.advancedsciencenews.com

**ADVANCED
ENERGY
MATERIALS**

www.advenergymat.de

Figure 3. a) Cycle number versus discharge capacity plots (potential range 2.00–4.95 V versus Li$^+$/Li) for the Fe-LIR sample, b) Corresponding voltage profiles for the 1st, 2nd, 4th, and 40th cycles.
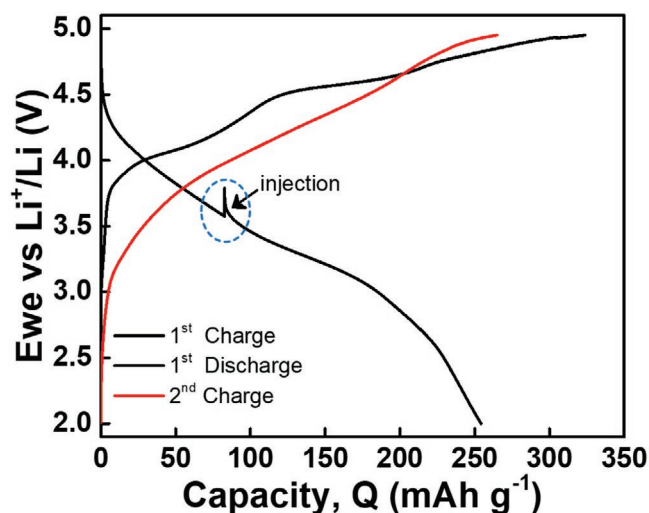

Figure 4. Voltage profiles of the first cycle and second charge of Li/Fe-LIR cell used for the XAS investigations done at C-rate C/10 in the voltage range 2.00–4.95 V versus Li$^+$/Li.

the potential of Mn^{4+}→Mn^{3+} electrochemical reaction to lower values. All these observations agree well with the cyclic voltammetry results displayed in Figure 2.

2.4. XAS Analysis

The first cycle and the second charge (C-rate C/10, potential range 2.00–4.95 V versus Li$^+$/Li) of the Fe-LIR were investigated using in operando XAS. The charge-discharge profiles of first cycle and the charging profile of the second cycle obtained during the in operando measurements are displayed in **Figure 4**.

The origin of the spike observed in the profile during the first discharge at ≈3.6 V is attributed to the pausing of the electrochemical experiment during the electron injection (40 min) at the synchrotron, resulting in a voltage relaxation. The obtained XAS results are summarized below:

2.4.1. Mn K Edge Investigations

Mn K edge XANES region of the XAS spectra of the pristine Fe-LIR sample looked identical to that of Li$_2$MnO$_3$ standard

material, indicating that geometry of the local coordination is identical and moreover, this short-range structural motif is representative for the whole material (see **Figure 5**a). This is in good agreement with the XRD results, where the superlattice reflections indicate the presence of a monoclinic phase (S.G. *C2/m*) corresponding to the Li-rich component. Nevertheless, significant difference is observed in the extended X-ray absorption fine structure (EXAFS) signals from both samples (Figure 5b), indicating the difference in the local coordination around Mn, possibly due to the incorporation of Ni and Fe atoms. As similar to Li$_2$MnO$_3$ or similar Li-rich Mn-containing cathode materials, Mn K edge XANES region of the present material is also characterized by a pre-edge absorption peak around 6540–6545 eV (peak "A"), having a doublet character and a shoulder "B" around 6549 eV, which is further followed by a strong absorption peak "C". The weak pre-edge peak "A" can be assigned to electric dipole-forbidden transition of a 1*s* electron to an unoccupied 3*d* orbital of a high spin octahedrally coordinated Mn atom, which is partially allowed because of the pure electric quadrupole coupling and/or the 3*d*-4*p* orbital mixing arising from the non-centrosymmetric environment of the slightly distorted octahedral 3*a* site in the rhombohedral $R\bar{3}m$ space group. The peak B, is assigned to the 1*s* to 4*p* transition involving a ligand-to-metal charge transfer (LMCT) or a *shake-down* process caused due to the deviation in the degeneracy of 4*p$_{xyz}$* orbital due to the distortion in the octahedra. The strongest absorption, peak C, is purely due to dipole-allowed 1*s*-4*p* transition without the *shake-down* process. During the electrochemical cycling process, characteristic changes occur to each of these peaks and careful interpretation is needed as structure involved with these class of Li-rich materials are so complicated as it involves contribution from Mn existing in two different phases.

The Mn K edge XANES spectra obtained during charging process are given in **Figure 6**a. During the charging process (removal of Li$^+$ from the Fe-LIR), the intensity of the pre-edge peak corresponding to Mn K edge (A) continuously increased. Moreover, with the onset of the charging process, splitting in
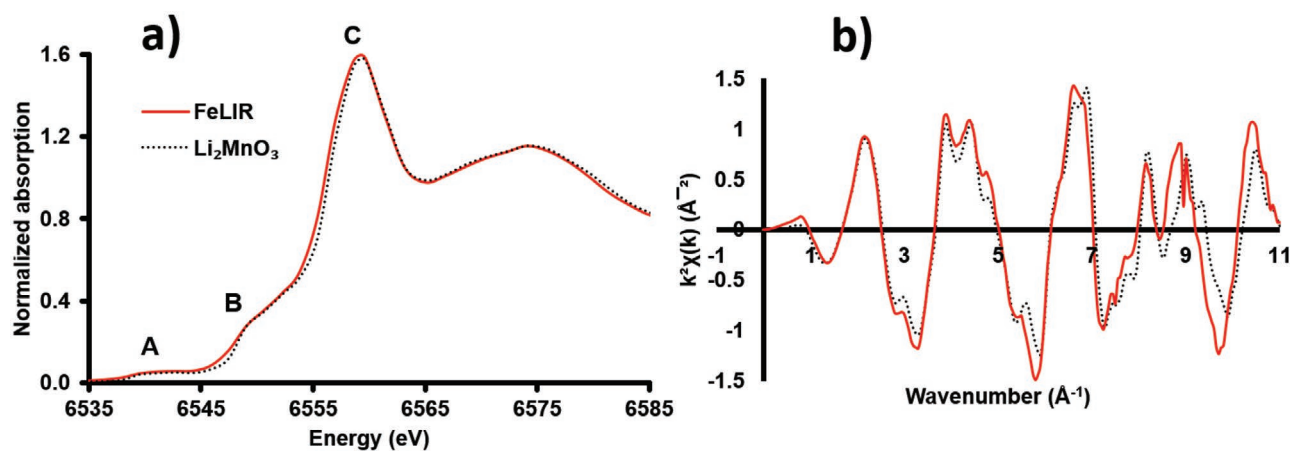
Figure 5. a) XANES Mn K edge comparison between the pristine Fe-LIR material and reference compound, b) corresponding k space, to highlight the difference in local coordination.

the pre-edge peak becomes less obvious. Once the cell potential reached nearly 4.5 V versus Li^+/Li, the doublet features merged forming a pre-edge peak without any splitting. This pre-edge peak attained the highest intensity at highest recorded cell potential or fully charged state. As mentioned before, the Mn K pre-edge is highly sensitive to the coordination environment of Mn. To get a clear picture, the pre-edge feature of the pristine, as well as fully charged state, are compared with pre-edge features of Mn reference materials MnO_2, Li_2MnO_3, and $LiMnO_2$ (Figure 6b). The background-subtracted pre-edge peaks of the reference compound, as well as the Fe-LIR sample, are shown in Figure 6c. Generally, the pre-edge intensity increases with increase in the oxidation state of Mn in the same coordination environment. Yet another factor influencing the intensity of the pre-edge of Mn coordinated in octahedral geometry is the size of the tunnel created by the edge and corner-sharing octahedra. When the edge-sharing octahedral chains are cross-linked by corners, tunnels are created, and depending on the size of the tunnel the pre-edge intensity varies. It is observed that the larger the tunnel size the lesser is the pre-edge intensity. On the other hand, when Mn is tetrahedrally coordinated, the pre-edge peak intensity corresponding to this Mn will be 4 to 7 orders higher than the Mn coordinated in octahedral environment. All these factors need to be considered when interpreting the pre-edge (of Mn K-edge) intensity of the Fe-LIR material. Among the chosen reference compounds, the Mn in both, MnO_2 and Li_2MnO_3 mainly exist as Mn^{4+}, however, small amount of Mn^{3+} (well below the detection limit of Mn K-edge XAS) can still be found in these compounds due to oxygen loss during the synthesis.[50] In $LiMnO_2$, Mn exists in Mn^{3+} oxidation state. Clearly, the position of the pre-edge maxima of the reference compound shifts to higher energy with increase in the amount of Mn^{4+} (assuming that almost all the Mn in MnO_2 exists as Mn^{4+}). As far as the intensity of the pre-edge peak is concerned, MnO_2/ pyrolusite sample showed the highest pre-edge intensity among the reference samples. This high intensity is due to the existence of smaller tunnels formed by sharing of the 8 corners and 2 edges of the oxygen octahedra. It is clear from Figure 6c that the pre-edge intensity of the Fe-LIR sample is higher than the MnO_2 reference. This observation could be correlated to the

formation of a MnO_2-like phase during the charging of Fe-LIR. Furthermore, it can be seen from Figure 6a that peak "B" corresponding to LMCT vanishes after 4.49 V and a new peak "B*" is formed at 6553 eV at fully charged state. The change in the peak "B" can be correlated to change in the electron density of the ligand, in this case, oxygen due to its partial oxidation. During the discharging process (Figure 6d), the pre-edge peak intensity decreases continuously. The reason could be the filling up of the tunnels in the MnO_2 phase with Li and the simultaneous reduction of some of the Mn^{4+} ions to Mn^{3+}. Concurrently, corresponding edge white line maxima shifted to lower energy, indicating a reduction in the oxidation state of Mn, that is, the formation of Mn^{3+}. Clearly, the XANES spectra obtained during the fully discharged state as well as the fresh sample differ considerably, indicating structural changes after first cycle.

One of the key questions to be addressed related to the cycling of the Li-rich material is quantifying the amount of Mn^{3+} at the end of discharge. Since XAS is a bulk average technique, quantification of one particular oxidation state of Mn is not straightforward as in the present system Mn exists in multiple phases. Furthermore, EXAFS analysis on such systems will be very challenging as large number of variables is required to fit the data. Under such situation, any bond distance obtained from the EXAFS analysis which should correlate to the oxidation state will be highly unreliable due to the high correlation among different variables in the EXAFS fitting. At fully discharged state it is expected that Mn exists in both Mn^{3+} and Mn^{4+} oxidation states, moreover, at this state of charge the amount of Mn^{3+} should be the highest. The Mn K-edge spectra at 2.10 V (fully discharged state) were compared with that of $LiMnO_2$ (Mn^{3+}) and Li_2MnO_3 (Mn^{4+}) and with experimentally weighted superposition of spectra. It can be seen that for the spectra corresponding to fully discharged state, the first pre-edge peak shifted to lower energy compared to Li_2MnO_3 and the pre-edge is still at higher energy compared to $LiMnO_2$. Moreover, the fully discharged spectra overlap with the experimentally weighted superposition of the spectra of $LiMnO_2$ and of Li_2MnO_3 in the weight ratio 4:6. Therefore, it may be concluded that almost 40% of Mn exists as Mn^{3+} at the end of discharge.

**ADVANCED
SCIENCE NEWS**

www.advancedsciencenews.com
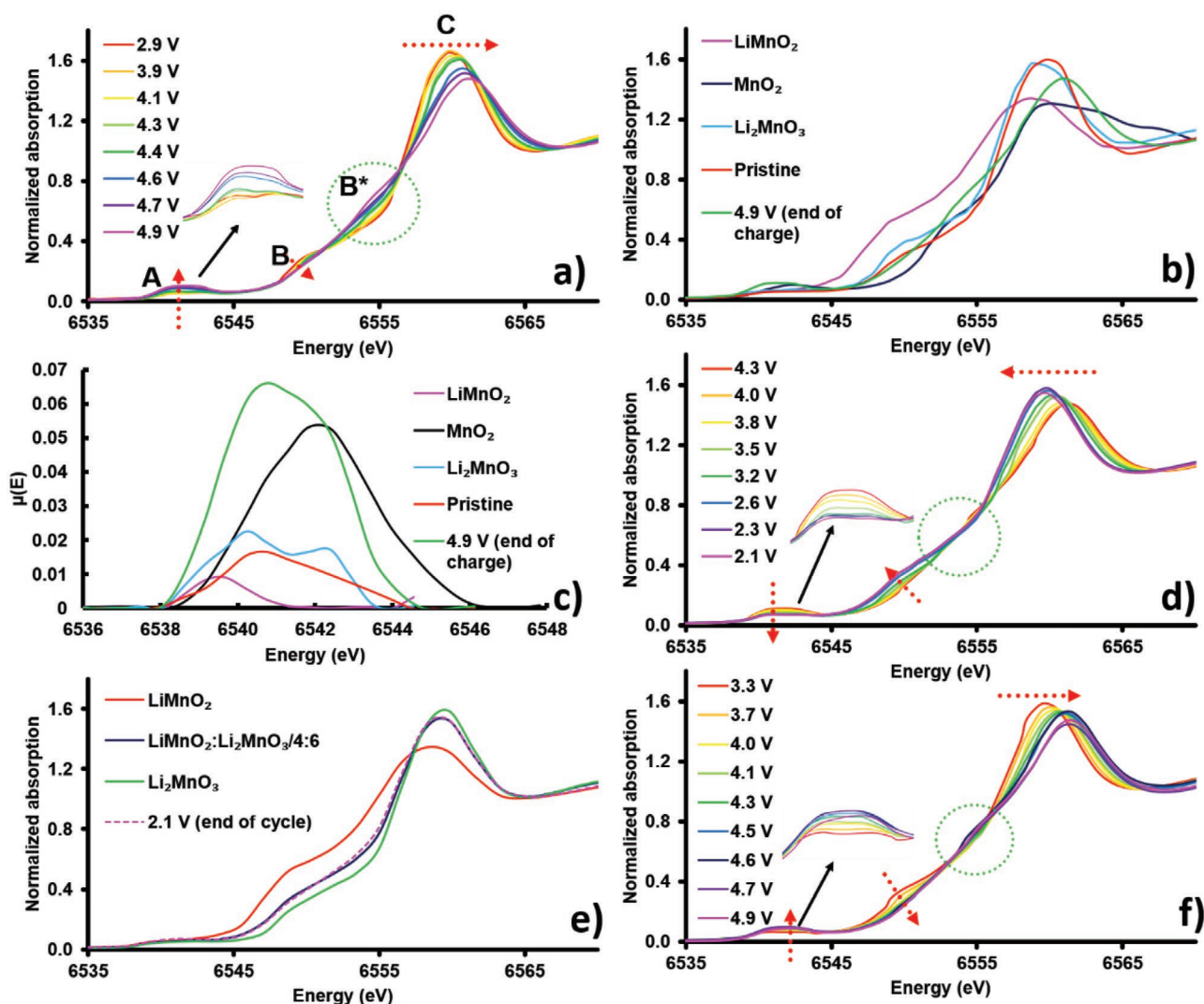
**ADVANCED
ENERGY
MATERIALS**

www.advenergymat.de

Figure 6. Fe-LIR; XANES Mn K edge a) during first charging, b) comparison of fully charged state with various reference compounds, c) background-subtracted pre-edge data, d) during discharging, e) estimation of Mn^{3+} in the fully discharged state, f) during second charging.

During the second charging, overall changes occurring to XANES spectra were similar to that of the first charging process. Like the first charging process, the pre-edge intensity of the Mn K edge increased throughout the charging window. Likewise, the peak maxima of the strongest absorption peak (C) continuously shifted to higher energy. Unlike the pristine sample, the changes occurring in the Mn K edge XANES during the second charging are partially due to the oxidation of Mn^{3+} to Mn^{4+}. Nevertheless, the pre-edge intensity corresponding to the fully charged state of the second charge cycle was slightly lower than the pre-edge intensity corresponding to the fully charged state of the first charge cycle. This indicates a reduced distortion of oxygen octahedra around the Mn. The Peak "B" corresponding to LMCT which is now having a maximum at lower energy compared to the fresh sample, also showed similar behavior. Similarly, during second charging, the peak "B" corresponding to LMCT vanished at a cell potential of 4.09 V versus Li^+/Li (much earlier than first charging) and peak "B*" is appearing at 6555 eV. As mentioned before peak "B*" can

be correlated to distortion associated change in electron density around the oxygen atom due to partial oxidation of oxygen.

2.4.2. Fe K Edge Investigations

Fe K edge XANES region of the XAS spectra of the pristine Fe-LIR sample is displayed in **Figure 7**.

In contrast to Mn K edge, the edge jump of the uncorrected spectra of the Fe XANES spectra was low due to the low amount of Fe in the Fe-LIR material. This is manifested by higher noise in the spectra, resulting from low amount of Fe in the sample as well as being within an electrochemical cell. Nevertheless, the XANES region has sufficient resolution for qualitative analysis. The Fe K edge XANES spectra of the Li-rich material almost overlapped with the spectra of reference compound $LiFeO_2$ indicating that Fe exists in 3+ oxidation state in the uncycled Li-rich compound. During the first charging, Fe K edge XANES spectra shifted to higher energy, till the cell reached 4.5 V versus
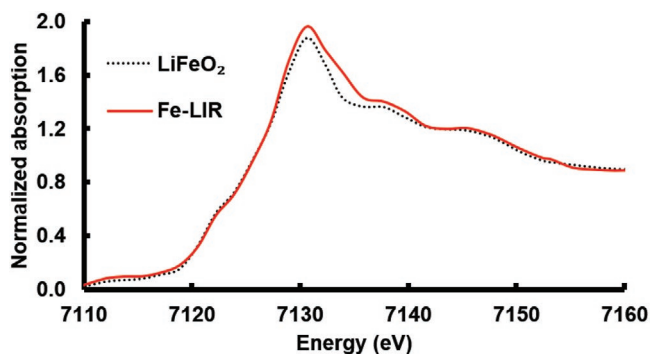
**ADVANCED
SCIENCE NEWS**

www.advancedsciencenews.com

**ADVANCED
ENERGY
MATERIALS**

www.advenergymat.de

Figure 7. Fe-LIR; XANES Fe K edge, comparison between the pristine material and reference compound $LiFeO_2$.

Li^+/Li (**Figure** 8a). This indicates the oxidation of Fe^{3+} to higher oxidation state say Fe^{4+}.[51] Upon further charging beyond 4.5 V versus Li^+/Li the edge region of the XANES spectra shifted continuously to lower energy (Figure 8b).

At fully charged state (4.9 V) the edge region almost overlapped with the edge region of the uncharged sample. Nevertheless, no shift in the position of the maxima of the white line was observed in this charging window. This unusual observation in the XANES spectra can be explained by the fact that the Fe is present in two oxidation states, that is, some of the Fe^{4+} formed during the charging process is reduced back to Fe^{3+}. This process can be further linked to the reductive coupling mechanism between oxygen and Fe metal resulting in the formation of peroxo/superoxo species and the reduction of Fe ions. This

reductive coupling mechanism between oxygen and 1) with Ru is reported in $Li_2Ru_{1-y}Sn_yO_3$ by Sathiya et al.,[52] 2) with Fe in Li_4FeSbO_6 by McCalla et al.[53] This reductive coupling mechanism can contribute to additional capacity which involves an irreversible deintercalation of Li^+. These Fe^{3+} ions formed could move into the vacant Li sites in the layers and may form spinel-like structure with continuous cycling. The quantity of Fe^{4+} during the fully charged state of Fe-LIR was relatively estimated using linear combination fitting (LCF) by choosing Fe K edge spectra obtained at 4.5 V versus Li^+/Li (highest amount of Fe^{4+} is expected at this potential and direct Fe^{4+} standards are rare) as well as alpha Fe_2O_3 (Fe^{3+}) as fitting components. The Fe K edge spectra obtained at the end of charge could be fitted (Figure S1a, Supporting Information) with 13% Fe_2O_3 along with contribution of 87% from Fe K edge spectra obtained at 4.5 V. Thus, it may be concluded that 13% of Fe was reduced in the charging potential window of 4.5 to 5.0 V versus Li^+/Li.

During discharging, the maxima of the white line shift to lower energies (see Figure 8c) and at the end of discharge, almost overlap with that of the uncycled material (Figure S1b, Supporting Information) indicating a completed reduction of Fe^{4+} to Fe^{3+}. However, XANES line shape, as well as white line intensity of the fully discharged state, differed slightly from the uncycled sample, indicating a change in coordination around the Fe ions. Thus, it is clear that both Mn and Fe coordination is influenced by charging beyond 4.5 V. XANES Fe K edge spectra recorded during the second charging behaved slightly differently from the first charging as the magnitude of shift of the XANES spectra to higher energy was smaller compared to the first charging process (Figure 8d). This difference in the
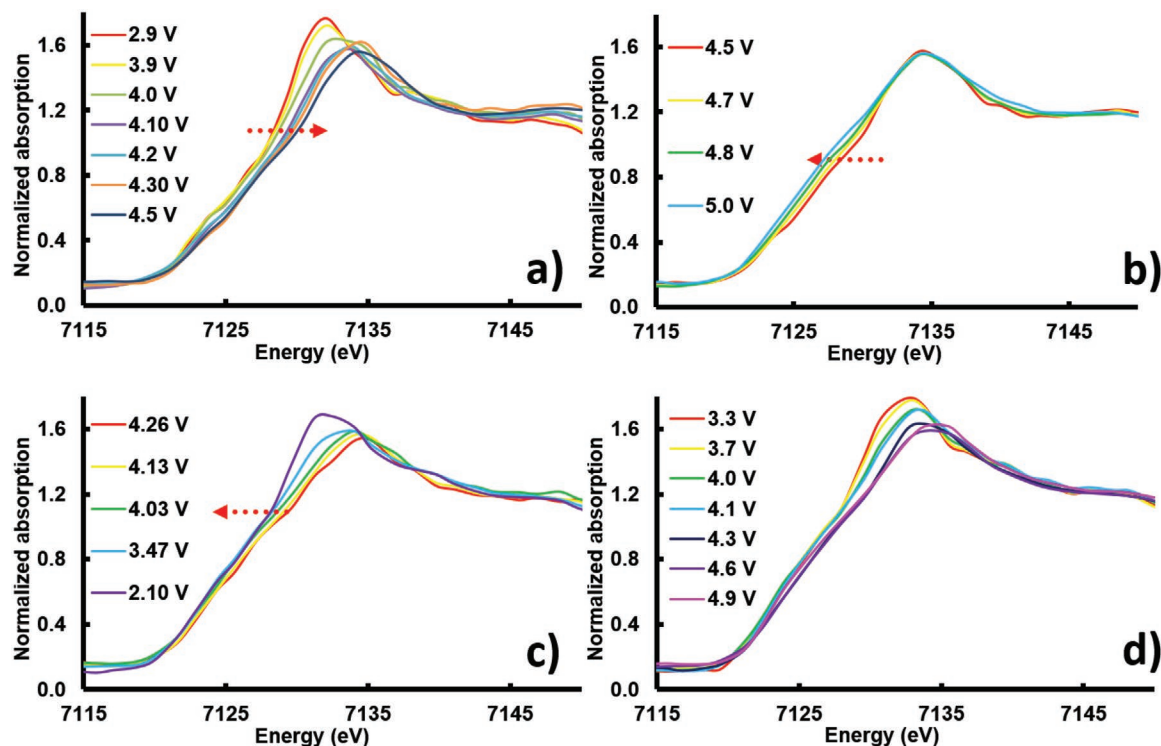

Figure 8. Fe-LIR; XANES Fe K edge a) during first charging, displaying oxidation of Fe^{3+} to Fe^{4+}, b) showing reductive coupling during first charging, c) during discharging, d) during second charging.
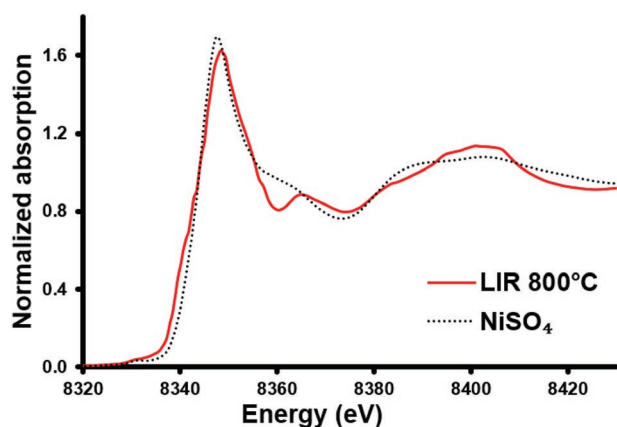
Figure 9. Fe-LIR; XANES Ni K edge, comparison between the pristine material, and reference compound $NiSO_4$.

electrochemical behavior can be correlated to the coordination change around Fe. Nevertheless, at fully charged state of the second charging, the position of the Fe K edge spectra shifted to lower energy, indicating reductive coupling similar to that of the first charging process but less pronounced.

2.4.3. Ni K Edge during Electrochemical Cycling

The Ni K edge XANES region of the XAS spectra of the pristine Fe-LIR sample is displayed in **Figure 9**. A comparison of the

obtained result with available reference material $NiSO_4$ reveals that Ni exists as Ni^{2+}.

The Ni K edge XAS spectra showed distinct changes with respect to charging window (**Figure 10**a). In general, XANES Ni K edge spectra shifted continuously to higher energy till the cell reached a potential of 4.5 V versus Li^+/Li. Between the potential window of 2.9 V (initial state) and 4.1 V versus Li^+/Li along with the edge shift, pronounced decrease in XANES white line intensity was observed. This decrease in the white line intensity can be correlated to the formation of Jahn-Teller distorted low-spin Ni^{3+} in between the charge cycle. Charging beyond 4.1 to 4.5 V versus Li^+/Li (Figure 10b), the absorption edge further shifted to higher energy, however, no significant change in the intensity of the white line was observed. Corresponding shift in the edge can be linked to oxidation of Ni^{3+} to Ni^{4+}. Interestingly, when the cell reached fully charged state (4.9 V versus Li^+/Li), a portion of the edge was shifted back to lower energy. This can be correlated to the reduction of a small fraction of Ni^{4+} which could be mediated by reductive coupling of Ni with oxygen, in other words, oxidation of surrounding oxygen atoms. A similar mechanism was also observed in an ex situ XAS investigation conducted on a P3-type Na-insertion cathode material $Na_{0.67}Ni_{0.2}Mn_{0.8}O_2$, as reported by Kim et al.[54] In order to estimate the oxidation state of Ni at the end of charge more precisely, the XANES Ni K edge spectra of Fe-LIR sample in the fully charged state is compared with Ni K edge spectra of fully charged states of $LiNi_{0.8}Co_{0.15}Al_{0.05}O_2$ (NCA) as well as $LiNi_{0.5}Mn_{1.5}O_4$ (LNMO) (Figure S2a, Supporting Information). Ni, in the fully charged states of both NCA and
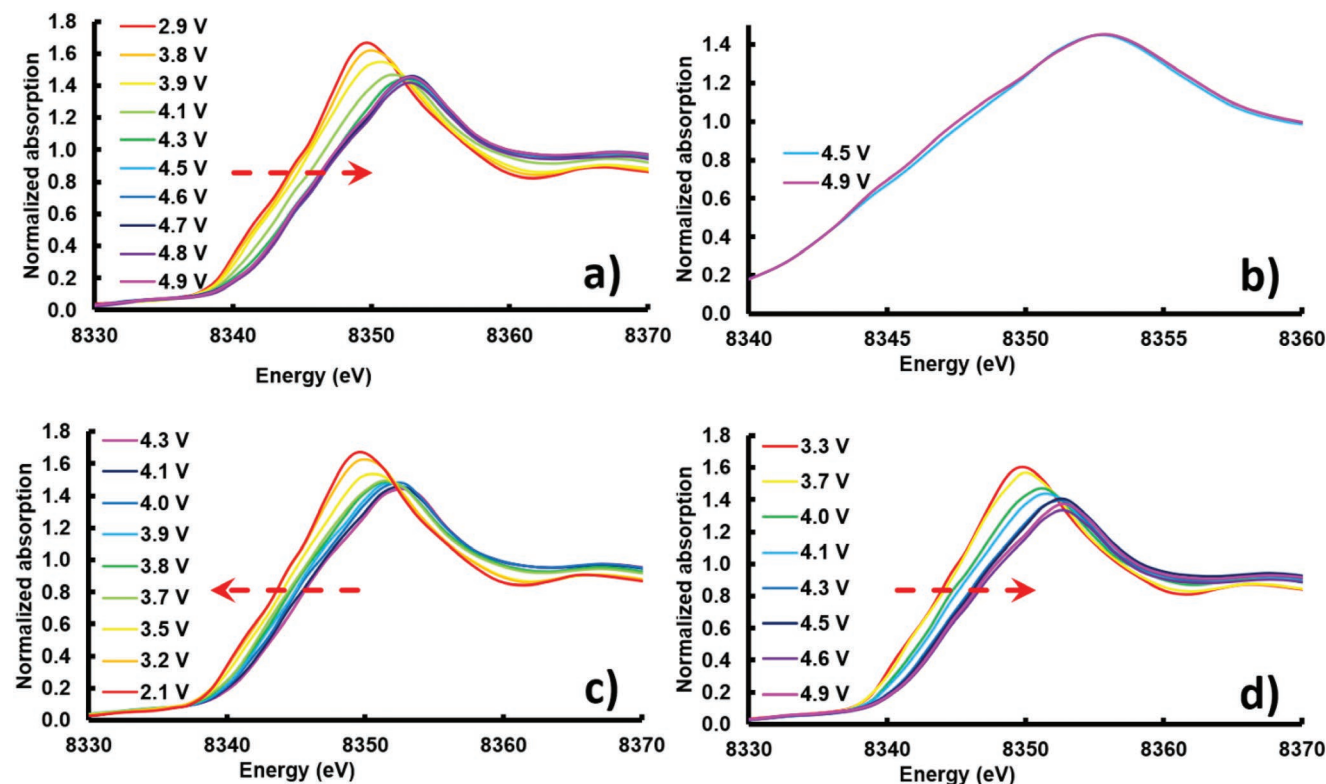

Figure 10. Fe-LIR; XANES Ni K edge a) during first charging, displaying oxidation of Ni^{2+} to Ni^{4+}, b) showing reductive coupling during first charging, c) during discharging, d) during second charging.

ADVANCED
SCIENCE NEWS
www.advancedsciencenews.com

ADVANCED
ENERGY
MATERIALS
www.advenergymat.de

LNMO (upper cut-off voltage of 4.2 and 5.0 V versus Li^+/Li, respectively) is expected to be in the +4 oxidation state.[55,56] From Figure S2a, Supporting Information, it is clear that Ni K edge spectra of the Fe-LIR sample at the end of charge are appearing at lower energy compared to that of fully charged NCA and LNMO, indicating a lower oxidation state for Ni in Fe-LIR sample at the end of charge. Further to estimate the oxidation state of Ni at the end of charge, LCF was carried out on the XANES Ni K edge spectrum of fully charged Fe-LIR sample, by using Ni K edge spectra of fully charged states of NCA and LNMO (Ni^{4+}) as well as fully discharged NCA (assuming that NCA predominantly contains Ni in its trivalent form) as fitting components, see Figure S2b, Supporting Information.[55] From the LCF it was concluded that 87% of Ni exist in tetravalent and the rest in trivalent oxidation states at the end of charge. The highest Ni^{4+} content (93%) was observed at potential of about 4.5 V versus Li^+/Li (see Figure S2c, Supporting Information) and therefore, it may be concluded that some of the Ni underwent reductive coupling, leading to the increase in amount of Ni^{3+} at end of charge.

In comparison to the charging process, XANES Ni K edge spectra continuously shifted to lower energies throughout the discharge process (Figure 10c). The difference in the trend of XANES patterns during the charging and discharging indicates that any Ni^{3+} formed at fully charged state due to reductive coupling does not revert back to Ni^{4+}. This also indicates that the reductive coupling between Ni and O during discharging proceeds through a different step compared to the reductive coupling during charging. Nevertheless, Ni K edge XANES spectra of the fully discharged state (after cycling), as well as the initial uncycled state, looked almost identical (see Figure S2d, Supporting Information). This provides evidence that unlike for Mn, the average local coordination around Ni was more or less preserved after cycling. During the subsequent charging process, the Ni K edge XANES spectra show a similar behavior to the first charging process (Figure 10d).

3. Conclusion

A cobalt-free Li-rich material with nominal composition $Li_{1.2}Mn_{0.56}Ni_{0.16}Fe_{0.08}O_2$ was synthesized using a citric acid assisted route. The obtained material exhibited layered Li-rich structure, with small amounts of a cubic spinel impurity phase. XAS investigations on the pristine sample revealed an average oxidation state distribution of Mn^{4+}, Fe^{3+}, and Ni^{2+} in $Li_{1.2}Mn_{0.56}Ni_{0.16}Fe_{0.08}O_2$. Simultaneous release of lithium and oxygen took place in the first charge during the electrochemical cycling of $Li_{1.2}Mn_{0.56}Ni_{0.16}Fe_{0.08}O_2$, as revealed by a steady plateau observed at >4.5 V versus Li^+/Li, resulting in delivering a huge first charge capacity of ≈315 mAh g^{-1}. In the subsequent discharge, the material exhibits a capacity of 243 mAh g^{-1}. After three formation cycles, the material still keeps on delivering a capacity >200 mAh g^{-1}, with a retention of 94% after 40 cycles, which makes it a potential cathode material for future applications. Additionally, revealing its electrochemical mechanism with in operando investigations would further help to tune the material. From the in operando XAS studies, it is clear that both Fe and Ni are involved in the reductive coupling as a result of the simultaneous release of oxygen and lithium, which contribute to the additional capacity observed in Li-rich materials, even though the mechanism could be different for each metal ion. From the intensity of the Mn K pre-edge, the formation of MnO_2 phase at fully charged state was confirmed, with a concurrent decrease in the Li_2MnO_3-like component. The intensity of the pre-edge peak increased, which could be correlated to the formation of tunnels (similar to the one found in MnO_2 reference material) formed with edge and corner-sharing octahedra. This MnO_2 phase was lithiated during the subsequent discharge cycle which was confirmed by the presence of Mn^{3+} (40%) in the fully discharged sample. From the Fe K edge XANES studies, the Fe^{3+} in the pristine material was found to be oxidized to Fe^{4+} during the charging. However, at fully charged state, a fraction of this Fe was found to be reduced back to Fe^{3+} due to the reductive coupling. Similar behavior was also observed in Ni K edge analysis, indicating that all the transition metals were involved in the reductive coupling. To conclude, $Li_{1.2}Mn_{0.56}Ni_{0.16}Fe_{0.08}O_2$ has multiple electrochemically active metal ions in it such as Fe, Ni, and Mn, which contributed to its anomalous first cycle capacity as well as capacities in the following cycles.

4. Experimental Section

Synthesis of the Layered Li-Rich Material $Li_{1.2}Mn_{0.56}Ni_{0.16}Fe_{0.08}O_2$: The layered Li-rich material with nominal composition, $Li_{1.2}Mn_{0.56}Ni_{0.16}Fe_{0.08}O_2$, was synthesized by a citric acid-assisted Pechini method and will be referred to as Fe-LIR hereafter where LIR stands for Li-rich.[57] As a first step, citric acid and ethylene glycol were mixed in a ratio of 1:4 to form a solution. Then the metal acetates (Aldrich > 98%) such as $C_4H_6MnO_4.4H_2O$, $C_4H_6NiO_4.4H_2O$, and $C_4H_6FeO_4$ were dissolved in the above solution at 90 °C by constant stirring. The obtained solution was then heated at 180 °C to evaporate excess ethylene glycol to form a gel which was then precalcined at 400 °C for 5 h (heating rate 5 °C min^{-1}) to obtain the initial precursor. The initial precursor was then ground in a mortar and was subjected to annealing at 800 °C for 10 h with a heating rate of 5 °C min^{-1}. The obtained sample was then ground in the mortar to obtain the final material.

Structural Characterization Using Synchrotron Diffraction: The crystal structure of the obtained powder was identified using synchrotron powder diffraction technique. A synchrotron powder diffraction dataset was collected at RT for the materials at the Powder Diffraction Beam Line (MSPD) at ALBA, Barcelona, using synchrotron radiation with an energy of 30 keV ($\lambda = 0.413486$ Å) and a MYTHEN 1D Position Sensitive Detector. In order to perform this experiment, the sample was filled in 0.5 mm Ø borosilicate capillaries. The capillary was rotated during the measurements to obtain better statistics. The structure refinement based on the observed diffraction data for the measured sample was performed by the Rietveld method with the aid of WinPLOTR package, containing FullProf program.[58] The estimated standard deviations of all refined parameters were calculated in agreement with Bérar and Lelann.[59]

Morphology Analysis: The morphology and particle size of the synthesized sample were characterized by SEM analysis using a Zeiss Supra 55 SEM (Scanning Electron Microscope) with primary electron energies of 5 and 15 keV and an in-lens detector.

Electrochemical Characterization: The Fe-LIR electrode was prepared by mixing 80% active material (w/w), 10% (w/w) Super C65 carbon and 10% (w/w) PVdF 6020 binder. The required components were mixed in *N*-methyl pyrrolidone (NMP) to obtain a homogeneous slurry which was then casted on aluminum foil right away using a doctor blade coater with a wet thickness of 150 μm. The coated foils were then dried at 80 °C at 12 h. Electrode discs of 12 mm were punched from the foil, pressed at 8 tons 1.3 cm^{-2}, and dried at 120 °C for 24 h in vacuum to

remove the residual NMP and traces of water to obtain electrodes of ≈3 mg. The prepared electrodes were then assembled in an Argon-filled glove box. The electrochemical investigations were performed using two-electrode Swagelok cells. Metallic lithium foil (Alfa Aesar with 10 mm diameter and 0.75 mm thickness, 99.9% metals basis) was utilized as the counter and reference electrode. A solution of 1 M LiPF$_6$ in EC: DMC, 1:1 (Merck) was used as electrolyte. In all experiments, a Whatman glass microfiber filter (thickness: 675 μm) with a diameter of 13 mm was used as separator and drenched with 200 μL of electrolyte. All the electrochemical experiments were performed at room temperature using a VMP multichannel potentiostatic–galvanostatic system (Biologic Science Instrument). All the potentials reported in this work refer to the Li$^+$/Li couple. The C-rates mentioned in the text were calculated considering 1 C as 250 mA g^{-1}.

In Operando and Ex Situ XAS Investigations: The bulk oxidation states of transition metals in as-synthesized Li-rich Li$_{1.2}$Mn$_{0.56}$Ni$_{0.16}$Fe$_{0.08}$O$_2$ material were investigated using ex situ XAS. For that, the sample was diluted with cellulose and pressed into a pellet. The prepared pellet was then placed into a multi-sample holder, aligned and the XAS spectra at Mn, Fe, and Ni K edges were recorded in transmission geometry. The electrochemical mechanism of the Fe-LIR electrode in a half-cell against Li metal counter electrode, for the first one-and-a-half cycle, was elucidated in operando using XAS. For this purpose, cells similar to those reported in previous work were used.[60,61] All the in operando and ex situ XAS measurements were carried out at the XAS beamline at Synchrotron Radiation Source at KIT, Karlsruhe, using a multiple sample changer.[61] In operando XAS spectra of Fe-LIR electrode were recorded in transmission geometry in Quick-EXAFS mode at Mn, Fe, and Ni K edges during electrochemical cycling. In order to measure Mn, Fe, and Ni edges in one run, the double crystal fixed exit monochromator equipped with Si (111) crystals as well as the ionization chamber (IC Spec Ionisation Chamber, Oxford) were aligned and optimized at 7.5 keV. To obtain reasonable time resolution, quick-EXAFS measurements were done with scan rate of 5 min for each spectrum. The spectra were processed using the Demeter software package based on IFEFFIT and FEFF.[62]

Supporting Information

Supporting Information is available from the Wiley Online Library or from the author.

Conflict of Interest

The authors declare no conflict of interest.

Data Availability Statement

Data available on request from the authors.

[1] J. Li, R. Klöpsch, M. C. Stan, S. Nowak, M. Kunze, M. Winter, S. Passerini, *J. Power Sources* **2011**, *196*, 4821.

[2] C. P. Laisa, A. K. Nanda Kumar, S. Selva Chandrasekaran, P. Murugan, N. Lakshminarasimhan, R. Govindaraj, K. Ramesha, *J. Power Sources* **2016**, *324*, 462.

[3] Z. Lu, L. Y. Beaulieu, R. A. Donaberger, C. L. Thomas, J. R. Dahn, *J. Electrochem. Soc.* **2002**, *149*, A778.

[4] M. M. Thackeray, C. S. Johnson, J. T. Vaughey, N. Li, S. A. Hackney, *J. Mater. Chem.* **2005**, *15*, 2257.

[5] M. M. Thackeray, S.-H. Kang, C. S. Johnson, J. T. Vaughey, R. Benedek, S. A. Hackney, *J. Mater. Chem.* **2007**, *17*, 3112.

[6] H. Yu, H. Zhou, *J. Phys. Chem. Lett.* **2013**, *4*, 1268.

[7] P. Kalyani, S. Chitra, T. Mohan, S. Gopukumar, *J. Power Sources* **1999**, *80*, 103.

[8] Y.-S. Hong, Y. J. Park, K. S. Ryu, S. H. Chang, M. G. Gyu, *J. Mater. Chem.* **2004**, *14*, 1424.

[9] J. Kim, C. S. Johnson, J. T. Vaughey, M. M. Thackeray, S. a Hackney, W. Yoon, C. P. Grey, *Chem. Mater.* **2004**, *16*, 1996.

[10] A. Ito, D. Li, Y. Ohsawa, Y. Sato, *J. Power Sources* **2008**, *183*, 344.

[11] F. Amalraj, D. Kovacheva, M. Talianker, L. Zeiri, J. Grinblat, N. Leifer, G. Goobes, B. Markovsky, D. Aurbach, *J. Electrochem. Soc.* **2010**, *157*, A1121.

[12] D. Kim, S.-H. Kang, M. Balasubramanian, C. S. Johnson, *Electrochem. Commun.* **2010**, *12*, 1618.

[13] Y. Jianhua, X. Liu, L. Bingyun, *RSC Adv.* **2014**, *4*, 63268.

[14] J. Li, J. Li, J. Luo, L. Wang, X. He, *Int. J. Electrochem. Sci.* **2011**, *6*, 1550.

[15] M. Tabuchi, Y. Nabeshima, M. Shikano, K. Ado, H. Kageyama, K. Tatsumi, *J. Electrochem. Soc.* **2007**, *154*, A638.

[16] M. Tabuchi, Y. Nabeshima, T. Takeuchi, H. Kageyama, K. Tatsumi, J. Akimoto, H. Shibuya, J. Imaizumi, *J. Power Sources* **2011**, *196*, 3611.

[17] Y. Zhao, G. Sun, R. Wu, *Electrochim. Acta* **2013**, *96*, 291.

[18] A. Manthiram, J. C. Knight, S.-T. Myung, S.-M. Oh, Y.-K. Sun, *Adv. Energy Mater.* **2015**, *6*, 1501010.

[19] T. R. Penki, D. Shanmughasundaram, B. Kishore, A. V. Jeyaseelan, A. K. Subramani, N. Munichandraiah, *J. Electrochem. Soc.* **2016**, *163*, A1493.

[20] Y. Zhao, Y. Wang, C. Ji, Z. Zhao, Z. Lv, *RSC Adv.* **2016**, *6*, 31762.

[21] J. N. Reimers, E. Rossen, C. D. Jones, J. R. Dahn, *Solid State Ionics* **1993**, *61*, 335.

[22] M. Tabuchi, A. Nakashima, H. Shigemura, K. Ado, H. Kobayashi, H. Sakaebe, H. Kageyama, T. Nakamura, M. Kohzaki, A. Hirano, R. Kanno, *J. Electrochem. Soc.* **2002**, *149*, A509.

[23] M. Tabuchi, A. Nakashima, K. Ado, H. Sakaebe, H. Kobayashi, H. Kageyama, K. Tatsumi, Y. Kobayashi, S. Seki, A. Yamanaka, *J. Power Sources* **2005**, *146*, 287.

[24] K. Karthikeyan, S. Amaresh, G. W. Lee, V. Aravindan, H. Kim, K. S. Kang, W. S. Kim, Y. S. Lee, *Electrochim. Acta* **2012**, *68*, 246.

[25] F. Lian, M. Gao, W. H. Qiu, P. Axmann, M. Wohlfahrt-Mehrens, *J. Appl. Electrochem.* **2012**, *42*, 409.

[26] G.-B. Liu, H. Liu, Y. Wang, Y.-F. Shi, Y. Zhang, *J. Solid State Electrochem.* **2013**, *17*, 2437.

[27] J. Li, L. Wang, L. Wang, J. Luo, J. Gao, J. Li, J. Wang, X. He, G. Tian, S. Fan, *J. Power Sources* **2013**, *244*, 652.

[28] P. K. Nayak, J. Grinblat, M. Levi, O. Haik, E. Levi, D. Aurbach, *J. Solid State Electrochem.* **2015**, *19*, 2781.

[29] G. B. Liu, H. Liu, Y. F. Shi, *Electrochim. Acta* **2013**, *88*, 112.

[30] T. R. Penki, D. Shanmughasundaram, N. Munichandraiah, *Electrochim. Acta* **2014**, *143*, 152.

[31] C.-C. Wang, A. Manthiram, *J. Mater. Chem. A* **2013**, *1*, 10209.

[32] W. C. West, J. Soler, M. C. Smart, B. V. Ratnakumar, S. Firdosy, V. Ravi, M. S. Anderson, J. Hrbacek, E. S. Lee, A. Manthiram, *J. Electrochem. Soc.* **2011**, *158*, A883.

[33] A. van Bommel, L. J. Krause, J. R. Dahn, *J. Electrochem. Soc.* **2011**, *158*, A731.

[34] J. Rana, M. Stan, R. Kloepsch, J. Li, G. Schumacher, E. Welter, I. Zizak, J. Banhart, M. Winter, *Adv. Energy Mater.* **2014**, *4*, 1300998.

[35] J. Rana, R. Kloepsch, J. Li, T. Scherb, G. Schumacher, M. Winter, J. Banhart, *J. Mater. Chem. A* **2014**, *2*, 9099.

[36] N. Tran, L. Croguennec, M. Ménétrier, F. Weill, P. Biensan, C. Jordy, C. Delmas, *Chem. Mater.* **2008**, *20*, 4815.

[37] K. Shimoda, K. Yazawa, T. Matsunaga, M. Murakami, K. Yamanaka, T. Ohta, E. Matsubara, Z. Ogumi, T. Abe, *Sci. Rep.* **2020**, *10*, 10048.

[38] E. Boivin, N. Guerrini, R. A. House, J. G. Lozano, L. Jin, G. J. Rees, J. W. Somerville, C. Kuss, M. R. Roberts, P. G. Bruce, *Adv. Funct. Mater.* **2021**, *31*, 2003660.

[39] C. Yin, L. Wan, B. Qiu, F. Wang, W. Jiang, H. Cui, J. Bai, S. Ehrlich, Z. Wei, Z. Liu, *Energy Storage Mater.* **2021**, *35*, 388.

[40] K. Nakahara, M. Tabuchi, S. Kuroshima, A. Toda, K. Tanimoto, K. Nakano, *J. Electrochem. Soc.* **2012**, *159*, A1398.

[41] J. Kikkawa, T. Akita, M. Tabuchi, M. Shikano, K. Tatsumi, M. Kohyama, *Electrochem. Solid-State Lett.* **2008**, *11*, A183.

[42] H. Koga, L. Croguennec, M. Ménétrier, P. Mannessiez, F. Weill, C. Delmas, *J. Power Sources* **2013**, *236*, 250.

[43] W. E. Gent, K. Lim, Y. Liang, Q. Li, T. Barnes, S.-J. Ahn, K. H. Stone, M. McIntire, J. Hong, J. H. Song, Y. Li, A. Mehta, S. Ermon, T. Tyliszczak, D. Kilcoyne, D. Vine, J.-H. Park, S.-K. Doo, M. F. Toney, W. Yang, D. Prendergast, W. C. Chueh, *Nat. Commun.* **2017**, *8*, 2091.

[44] R. Yuge, A. Toda, S. Kuroshima, H. Sato, T. Miyazaki, M. Tabuchi, K. Nakahara, *J. Electrochem. Soc.* **2014**, *161*, A2237.

[45] M. Oishi, K. Yamanaka, I. Watanabe, K. Shimoda, T. Matsunaga, H. Arai, Y. Ukyo, Y. Uchimoto, Z. Ogumi, T. Ohta, *J. Mater. Chem. A* **2016**, *4*, 9293.

[46] R. Satish, K. Lim, N. Bucher, S. Hartung, V. Aravindan, J. Franklin, J.-S. Lee, M. F. Toney, S. Madhavi, *J. Mater. Chem. A* **2017**, *5*, 14387.

[47] J. Xu, M. Sun, R. Qiao, S. E. Renfrew, L. Ma, T. Wu, S. Hwang, D. Nordlund, D. Su, K. Amine, J. Lu, B. D. McCloskey, W. Yang, W. Tong, *Nat. Commun.* **2018**, *9*, 947.

[48] L. Riekehr, J. Liu, B. Schwarz, F. Sigel, I. Kerkamm, Y. Xia, H. Ehrenberg, *J. Power Sources* **2016**, *306*, 135.

[49] A. Bhaskar, S. Krueger, V. Siozios, J. Li, S. Nowak, M. Winter, *Adv. Energy Mater.* **2015**, *5*, 1401156.

[50] X. Zhang, D. Luo, G. Li, J. Zheng, C. Yu, X. Guan, C. Fu, X. Huang, L. Li, *J. Mater. Chem. A* **2013**, *1*, 9721.

[51] C. Dräger, F. Sigel, R. Witte, R. Kruk, L. Pfaffmann, S. Mangold, V. Mereacre, M. Knapp, H. Ehrenberg, S. Indris, *Phys. Chem. Chem. Phys.* **2019**, *21*, 89.

[52] M. Sathiya, G. Rousse, K. Ramesha, C. P. Laisa, H. Vezin, M. T. Sougrati, M.-L. Doublet, D. Foix, D. Gonbeau, W. Walker, A. S. Prakash, M. Ben Hassine, L. Dupont, J.-M. Tarascon, *Nat. Mater.* **2013**, *12*, 827.

[53] E. McCalla, M. T. Sougrati, G. Rousse, E. J. Berg, A. Abakumov, N. Recham, K. Ramesha, M. Sathiya, R. Dominko, G. Van Tendeloo, P. Novák, J.-M. Tarascon, *J. Am. Chem. Soc.* **2015**, *137*, 4804.

[54] E. J. Kim, L. A. Ma, L. C. Duda, D. M. Pickup, A. V. Chadwick, R. Younesi, J. T. S. Irvine, A. R. Armstrong, *ACS Appl. Energy Mater.* **2020**, *3*, 184.

[55] Z. W. Lebens-Higgins, N. V. Faenza, M. D. Radin, H. Liu, S. Sallis, J. Rana, J. Vinckeviciute, P. J. Reeves, M. J. Zuba, F. Badway, N. Pereira, K. W. Chapman, T.-L. Lee, T. Wu, C. P. Grey, B. C. Melot, A. Van Der Ven, G. G. Amatucci, L. F. J. Piper, *Mater. Horiz.* **2019**, *6*, 2112.

[56] J. Rana, S. Glatthaar, H. Gesswein, N. Sharma, J. R. Binder, R. Chernikov, G. Schumacher, J. Banhart, *J. Power Sources* **2014**, *255*, 439.

[57] A. Bhaskar, N. N. Bramnik, A. Senyshyn, H. Fuess, H. Ehrenberg, *J. Electrochem. Soc.* **2010**, *157*, A689.

[58] T. Roisnel, J. Rodríguez-Carvajal, *Mater. Sci. Forum* **2001**, *118*, 378

[59] J.-F. Bérar, P. Lelann, *J. Appl. Crystallogr.* **1991**, *24*, 1.

[60] M. Herklotz, F. Scheiba, M. Hinterstein, K. Nikolowski, M. Knapp, A. C. Dippel, L. Giebeler, J. Eckert, H. Ehrenberg, *J. Appl. Crystallogr.* **2013**, *46*, 1117.

[61] G. Balachandran, D. Dixon, N. Bramnik, A. Bhaskar, M. Yavuz, L. Pfaffmann, F. Scheiba, S. Mangold, H. Ehrenberg, *ChemElectroChem* **2015**, *2*, 1510.

[62] B. Ravel, M. Newville, *J. Synchrotron Radiat.* **2005**, *12*, 537.